





# Analysis of Scalable Electromagnetically-Modeled Anomalous Reflectors through Ray Tracing and Measurements

LE HAO <sup>1</sup> (Member, IEEE), SRAVAN KUMAR REDDY VUYYURU <sup>2,3</sup> (Member, IEEE),  
SERGEI A. TRETYAKOV <sup>3</sup> (Fellow, IEEE), MARKUS RUPP <sup>1</sup> (Fellow, IEEE), AND  
RISTO VALKONEN <sup>2</sup> (Member, IEEE)

<sup>1</sup>Institute of Telecommunications, Technische Universität Wien (TU Wien), 1040 Vienna, Austria.

<sup>2</sup>Nokia Bell Labs, 02610 Espoo, Finland

<sup>3</sup>Department of Electronics and Nanoengineering, School of Electrical Engineering, Aalto University, 02150 Espoo, Finland

CORRESPONDING AUTHOR: Le Hao (e-mail: le.hao@tuwien.ac.at).

This work was supported in part by the European Union's Horizon 2020 MSCA-ITN-METAWIRELESS project, under the Marie Skłodowska-Curie grant agreement No. 956256, in part by the Vienna Science and Technology Fund (WWTF) [Grant ID: 10.47379/VRG23002], in part by the Research Council of Finland within the RCF-DoD Future Information Architecture for IoT initiative, grant No. 365679, in part by the Nokia Foundation, and in part by the HPY Research Foundation. The authors acknowledge TU Wien Bibliothek for financial support through its Open Access Funding Program.

**ABSTRACT** In this study, we elaborate on the concept of a scalable anomalous reflector to analyze the angular response, frequency response, and spatial scalability of a designed anomalous reflector across a broad range of angles and frequencies. We utilize theoretical models and ray tracing simulations to investigate the communication performance of two different-sized scalable finite anomalous reflectors, one smaller configuration with  $48 \times 48$  array of unit cells and the other constructed by combining four smaller anomalous reflectors to form a larger array with  $96 \times 96$  unit cells. To validate the theoretical approach developed, we conducted measurements in an auditorium to evaluate the received power through an anomalous reflector link at different angles and frequencies. In addition, models of scalable deflectors are implemented in the MATLAB ray tracer to simulate the measurement scenario. The results from theoretical calculations and ray tracing simulations show good agreement with the measurement results. The proposed models and parameter abstractions for electromagnetically modeled anomalous reflectors are generalizable and applicable to various types of anomalous reflectors and reconfigurable intelligent surfaces, offering potential benefits for efficient cellular network planning in wireless communications.

**INDEX TERMS** Anomalous reflector, measurement, ray tracing, reconfigurable intelligent surface, 6G.

## I. Introduction

**A**NOMALOUS reflectors (ARs) with dense two-dimensional grids of subwavelength unit cells have gained attention in the realization of the deflection of incident waves towards the desired directions [1]–[14]. To achieve such performance, the electromagnetic (EM) properties of each unit cell are controlled. The initial research on ARs based on conventional methods [15], [16], violating the usual reflection law (i.e., the incident and reflection angles are unequal,  $\theta_i \neq \theta_r$ ) suffers from lower efficiencies for anomalous reflection angles beyond  $45^\circ$ , e.g. [1]. Extensive research on ARs established advanced design methods using

periodic reflectors because only one period needs to be analyzed and designed, resulting in highly efficient anomalous reflectors at a steep angle, e.g. [2], [3] or multichannel reflectors [12], [13], and researchers work on developing scanning capabilities of these devices.

Although extensive research has been carried out in modeling reconfigurable intelligent surface (RIS)-assisted communication links with anomalous reflection functionality in the past years, the current research usually focuses on the EM macroscopic parameters of ARs, such as the anomalous reflection efficiency and scattering pattern, significantly lacking comprehensive analysis of communication aspects in

realistic environments [17]–[21]. Further research is needed to incorporate these models into network simulators. Moreover, most existing studies on the communication aspects of AR rely on simplified or even idealized models that lack validation against realistic AR designs based on the EM theory [22], [23]. Additionally, there is a deficiency in research addressing the frequency selectivity and spatial scalability of ARs. The model in [10] utilized macroscopic reflection coefficients to capture multiple Floquet harmonics but is limited to periodic metasurfaces and neglects diffuse scattering from imperfections and panel edges. The model in [24], [25] enables ray-based simulation by accounting for multimode reradiation and diffuse scattering from finite-size RISs, but the integration of key EM characteristics, such as anomalous reflection efficiency and scattering patterns, remains limited.

Developing and validating accurate macroscopic models are significant for the design and performance evaluation of RIS-assisted communication systems. This paper addresses the above limitations, and the contributions can be summarized as follows:

- The macroscopic EM parameters of a manufactured, EM-designed AR are integrated into distinct communication models and software packages commonly used in communication system modeling.
- Large-scale fading in AR-assisted communication links is analytically characterized and simulated using ray tracing in realistic indoor scenarios with the manufactured AR.
- Theoretical predictions and ray tracing model simulations are compared and verified by empirical measurements.
- This study analyzes the angular and frequency response of a manufactured 3-bit AR in communication models through ray tracing and measurements in an indoor environment.
- The scalability of the manufactured AR is analyzed by tiling multiple small AR panels into a larger-size AR.
- Since the AR is accurately modeled and validated in a ray tracing framework, the proposed modeling approach becomes generalizable and can be reused for different ARs. By utilizing AR's scattering patterns, ray tracing can accurately predict the communication link performance in complex environments, eliminating the need for repeated physical site-specific measurements.

The remainder of this article is organized as follows: Section II briefly introduces the designed and manufactured AR along with its validated scattering pattern. Section III presents two theoretical path loss models for AR-assisted links. Section IV describes the measurement system, including the measurement scenario and setups. Section V explains the ray tracing simulation procedures with the AR in the MATLAB ray tracer. Section VI compares results from the theoretical models, ray tracing simulations, and measure-

ments for two ARs of different sizes. Finally, conclusions are formulated in Section VII.

## II. Scalable Anomalous Reflector: EM-Consistent Design and Manufacturing Strategy

To analyze the frequency selectivity and scalability of ARs in realistic communication systems, this work adopts the design methodology proposed in [3], [13], employing synthesis and manufacturing techniques to develop scalable ARs. In [13], we introduce a reconfigurable anomalous reflector enabled by an algebraic array antenna scattering synthesis technique to optimize the scattering characteristics of passively loaded periodic arrays of patch elements. Using the load impedances as the optimization variables for the scattering synthesis problem replaces heavy computations with supercell-level optimization. The infinite array of flat multimode electrically large supercells reflects normally incident waves into one of nine reflection directions, set to  $0^\circ$ ,  $\pm 13^\circ$ ,  $\pm 27^\circ$ ,  $\pm 43^\circ$ , and  $\pm 65^\circ$ , without parasitic scattering. The supercell dimension, determined from the Floquet-Bloch theory, is  $d = 4\lambda / |\sin \theta^{r,\max}|$ , where the maximum desired deflection direction is  $\theta^{r,\max} = 65^\circ$ . The distance between unit cells in supercells is set to  $d/16$ , that is, each supercell contains 16 unit cells. By optimizing the load impedance of each unit cell using the array antenna scattering synthesis technique described in [13], the reflected wave from a finite-size panel is focused in the desired main direction, while parasitic scattering in other directions is effectively suppressed.

Following this design technique, a 3-bit static AR prototype is manufactured. It reflects normally incident waves into  $65^\circ$  at the center frequency of 26 GHz, with 3-bit quantization resolution for reactive loads being sufficient. The design technique accounts for mutual coupling between elements, reradiated scattering, directional characteristics, structural scattering, and possible parasitic scattering, which is essential for developing EM-consistent and accurate wireless network modeling. While [13] focused on the AR design methodology and scattering properties of the AR to generate macroscopic parameters, and [14] connected the EM analysis and communication models for a perfectly functioning RIS, this work employs the same AR prototype to validate communications models for a realistic, lossy AR through ray tracing simulations and measurements. Furthermore, we assess its frequency response and scalability.

The manufactured AR prototype consists of  $48 \times 48$  identical unit cells, each with a dimension of  $0.2758\lambda \times 0.2758\lambda$ , resulting in a prototype size of  $152.6 \text{ mm} \times 152.6 \text{ mm}$ , as illustrated in Fig. 1. Each unit cell is constructed by a copper square patch applied on top of a printed circuit board (PCB) which uses Rogers RO4350B (LoPro) laminate with a 0.55 mm thickness ( $\epsilon_r = 3.66$ ,  $\tan \delta = 0.0037$ ). Each unit cell within a supercell is loaded with a reactive impedance implemented by shorted or open coplanar lines, optimized through simulation-based synthesis described in [13]. For convenience of our analysis, we reformulate the results

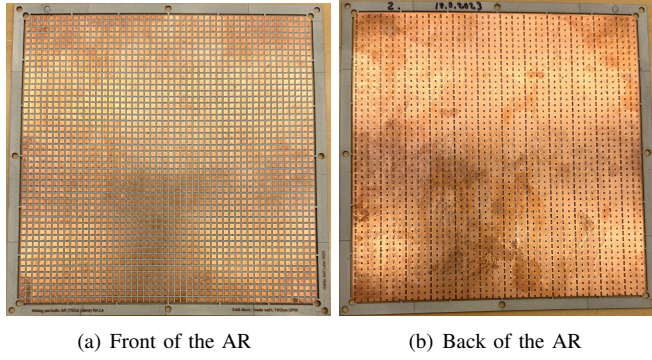


**FIGURE 1.** A 3-bit manufactured, non-reconfigurable AR prototype with  $48 \times 48$  identical unit cells, each measuring  $0.2758\lambda \times 0.2758\lambda$  at 26 GHz, resulting in overall prototype dimensions of  $13.24\lambda \times 13.24\lambda$ .

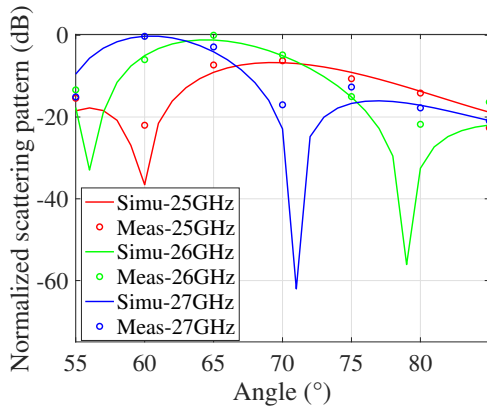


**FIGURE 2.** Normalized scattering pattern of the  $48 \times 48$ -sized AR at different frequencies and angles from CST simulation and measurement.

of the measured and simulated scattering pattern of this AR in Fig. 2. The scattering values are normalized to the maximum power. It should be mentioned that the AR was originally designed only for 26 GHz, but the results indicate that it also works well at 25 and 27 GHz, with the main reflection direction shifted by  $5^\circ$ . For example, the main reflection direction occurs at  $70^\circ$ ,  $65^\circ$ , and  $60^\circ$  when the frequency changes from 25 GHz to 27 GHz. It demonstrates good agreement between the measurement results and CST simulations in the main beam direction at 25, 26, and 27 GHz. As frequency increases, the reflection angle decreases since the anomalous reflection angle depends on the frequency according to  $\lambda \propto \sin \theta^r$  for normal incidence. Minor deviations are attributed to discrepancies between the assumed and actual material parameters.

### III. Path loss models

Different path loss models for ARs based on EM and communication models have been discussed in [26]. To investigate the communication performance of AR-assisted links, selecting an appropriate and accurate path loss model is crucial. This section introduces two different path loss models for AR-assisted links, referred to as Method 1 and Method 2.

For periodic metasurfaces, the distribution of scattered fields over all angles can be estimated based on the results of Section II in [27], also for imperfect ARs that produce some parasitic scattering into undesired Floquet modes. The propagation of signals due to reflections from some objects is conventionally modeled in terms of the bi-static scattering cross section that can be determined based on the analytical model in [27]. Due to its simple analytical formula for reflections in the desired direction, we use this model as the first method for a theoretical analysis of our manufactured AR. The received power estimated by Method 1 is given by

$$P_1 = P_t G_t G_r \eta_{\text{eff}} \left( \frac{S_1}{4\pi R_1 R_2} \right)^2 |\cos \theta_i \cos \theta_r|, \quad (1)$$

where  $P_t$  denotes the transmitted power at the transmitter (Tx);  $G_t$  and  $G_r$  represent the antenna gains at the Tx and receiver (Rx), respectively. The aperture size of the AR is denoted as  $S_1$ , and  $0 < \eta_{\text{eff}} \leq 1$  is a compensation parameter that takes into account the design and manufacturing imperfections of the AR;  $R_1$  and  $R_2$  denote the distances from the Tx to the AR and from the AR to the Rx, respectively. The angles  $\theta_i$  and  $\theta_r$  are the incidence and reflection angles, measured from the normal to the AR.

For the integration of the AR models into ray tracing simulators, it is more convenient to use the model of the scattering performance of AR in terms of the AR panel gains in the directions of illumination and observation [26], which we call Method 2. This approach is based on the Friis formula and gives the received power estimation

$$P_2 = \frac{P_t G_t G_{\text{rx}} G_{\text{tx}} \lambda^4}{(4\pi)^4 (R_1 R_2)^2}. \quad (2)$$

Here,  $G_{\text{rx}}$  is the gain of the AR in the direction from AR to Tx, and  $G_{\text{tx}}$  is the gain in the direction from AR to Rx. They are obtained from the CST simulation of the AR, where we first calculate the directivity of the AR (denoted as  $D_i$ ) from the far-field pattern in the CST simulation. Next, we use the directivity value to approximate the gain of the AR according to  $G = e_{\text{cd}} D_i$  [28] and assume the panel efficiency  $e_{\text{cd}} = 1$ . This theoretical model combines analytical estimations of the propagation loss with the radiation pattern results from EM simulations. By using the simulated AR gain at different angles, we can obtain received power results at the corresponding angles. Note that (2) is the same as (6) in [29], but here we use it for the whole AR panel and not for a single array element, as in [29]. Finally, we note that the product of the two gains of the AR panel is related to its bi-static scattering cross-section  $\sigma$  as

$$G_{\text{rx}} G_{\text{tx}} = \frac{4\pi\sigma}{\lambda^2}, \quad (3)$$

which is a function of both angles of incidence and observation. This equation establishes the relation between the results given by the two methods used. It is important to note that Method 1 is a purely theoretical model that assumes that the currents induced at a finite-size panel are the same as on an infinite ideally functioning anomalous reflector





FIGURE 3. Measurement scenario and equipment.

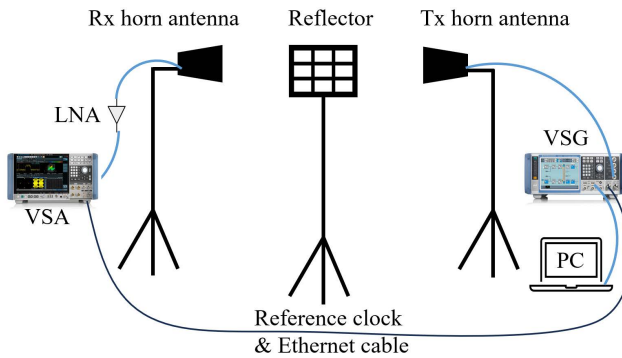


FIGURE 4. Measurement setup.

(with perfectly suppressed parasitic scattering), neglecting the edge effects. In contrast, Method 2 incorporates EM simulation data, making it more suitable for accurately modeling realistic, lossy ARs.

#### IV. Measurement System

This section presents over-the-air measurement results obtained in an auditorium, both with and without the manufactured AR prototypes, to evaluate the communication performance of the ARs, i.e., the large-scale fading through the Tx-AR-Rx link. We first introduce the measurement scenario and setup, including the measurements between the Tx and the Rx antennas without AR as a reference for calibration. Next, we explain the measurements with ARs for the Tx-AR-Rx links while the direct Tx-Rx link is blocked. In the measurement, two different-sized ARs are tested to assess the scalability of the AR. The first one is the original small AR with  $48 \times 48$  unit cells. The second one is a manually combined larger AR from four identical pieces of the  $48 \times 48$ -sized AR; thus, it consists of  $96 \times 96$  unit cells with a dimension of  $305.3 \text{ mm} \times 305.3 \text{ mm}$ . Specifically, copper tape is used to glue the edges of the four small AR pieces to ensure continuous alignment of neighboring elements in the same plane, minimizing misalignment. The combined  $96 \times 96$ -sized AR is displayed in Fig. 3(c).

TABLE 1. MEASUREMENT PARAMETERS

	Item	value
Transmitted power	$P_t$	6 dBm
Cable loss at Tx side	$(-L_t)$	-2.5 dB
Tx antenna gain	$G_t$	18 dBi
Rx antenna gain	$G_r$	18 dBi
LNA gain + cable loss at Rx side	$G_a$	19.9 dB
Distance between the Tx and AR	$R_1$	5.5 m
Distance between the Rx and AR	$R_2$	7 m

#### A. Measurement scenario and setups

The measurement was conducted in a  $14 \times 8 \times 3 \text{ (m}^3\text{)}$  sized auditorium at the Nokia Bell Labs office in Espoo, Finland. As shown in Fig. 3, the Tx and Rx antennas are the same horn antennas with a maximum gain of 18 dBi and a beamwidth of  $22^\circ$ . We fix the positions of the AR and the Tx antenna with a distance of 5.5 m between them. Then we move the Rx antenna to  $55^\circ, 60^\circ, 65^\circ, 70^\circ, 75^\circ, 80^\circ$ , and  $85^\circ$  from the AR, respectively, and keep the distances between them to be always 7 m. The heights of the Tx, Rx, and the AR center are 1.5 m.

The measurement setup is shown in Fig. 4. The Tx horn antenna is connected to an R&S vector signal generator (VSG) SMW200A and then to a control computer. The VSG generates a 5G NR signal with a transmitting power of +6 dBm. The Rx horn antenna is connected to a low-noise amplifier (LNA) Miteq JS4 and then connected to an R&S FSW vector signal analyzer (VSA). The VSA is connected to the VSG via an Ethernet cable and reference clock for synchronizing. The setup parameters are listed in Table 1.

In the measurement, we transmit 16 QAM or 64 QAM orthogonal frequency-division multiplexing (OFDM) modulated signals with a channel bandwidth of 400 MHz or 100 MHz, respectively. Then we measure the error vector magnitude (EVM) and received power at the Rx side. EVM is a parameter for evaluating the conditions of the received signal demodulation, and we use it to indicate the received signal quality. Since this kind of measurement takes a long

**TABLE 2. POWER DIFFERENCES BETWEEN THEORY AND MEASUREMENTS**

$P_{\text{diff}}$ (dB)	55°	60°	65°	70°	75°	80°	85°
25 GHz	0.87	0.78	0.77	0.25	0.14	0.28	1.52
26 GHz	1.46	1.55	1.08	0.68	0.26	1.05	0.28
27 GHz	1.04	2.13	1.56	1.33	1.79	−0.04	1.85

time with the used instrumentation, we measure only at three distinct frequencies, i.e., 25, 26, and 27 GHz with the modulated signals. For reference, we use a continuous wave signal sweeping from 24.5 GHz to 27.5 GHz with a step of 0.25 GHz to have proper frequency responses and a quicker measurement setup.

### B. Reference measurement without the AR

To obtain accurate measurement results and have a fair comparison with simulation results, we first conduct a reference measurement with only line-of-sight (LoS) links between the Tx and the Rx antenna. Next, we compare the measured results with theory to find out how much power difference we obtain between them. During the measurement, we fix the Tx antenna position and move the Rx antenna to the above-mentioned 7 different locations from 55° to 85°. At each Rx location, we orient the Tx and Rx antennas to align their main beam directions toward each other, and we measure the received power at the Rx antenna through the LoS path from the Tx antenna. We conduct the measurement first with 16 QAM-modulated waves at 25, 26, and 27 GHz, then we use continuous waves to sweep from 24.5 GHz to 27.5 GHz with 0.25 GHz step.

We denote the measured received power value as  $P_m$ . Then we calculate the free space path loss between the Tx and the Rx using the Friis formula  $P_{\text{FSPL}} = \left(\frac{\lambda}{4\pi R_3}\right)^2$  in W, where  $R_3$  denotes the distances between the Tx and Rx antennas. The final calculated received power from theory is  $P_{\text{theory}} = P_t + G_t + G_r + P_{\text{FSPL}} - L_t + G_a$  in dBm. The parameters  $P_t$ ,  $G_t$ ,  $G_r$ ,  $L_t$ , and  $G_a$  denote the transmitted power, Tx antenna gain, Rx antenna gain, cable loss at the Tx side, and LNA gain together with the Rx cable loss, respectively. The values can be found in Table 1. The power difference between the theoretical and measurement results is  $P_{\text{diff}} = P_{\text{theory}} - P_m$  in dB. For modulated-wave measurement, we only use the results at 25, 26, and 27 GHz, while for continuous-wave measurement, we use values at all frequencies to calculate the power difference.

In Table 2, we list the  $P_{\text{diff}}$  with modulated measurement results at the three frequencies. These small differences may come from the losses in the measurement system that we could not count in our model. The losses due to measurement devices may have a little deviation between the measurement and simulation. For instance, when we perform measurements at different frequencies, the antenna gain has about  $\pm 0.5$  dB variability. The LNA gain and the Rx cable loss together have about 1.6 dB variation, and the Tx cable

loss has around 0.065 dB variability in the frequency range. However, in the simulation, we use the same values for these losses. When we take this  $P_{\text{diff}}$  into account and use it to correct the calculated and simulated results with the AR, we can eliminate the influence of these factors and obtain more accurate correspondence between the simulation model and the measurement.

### C. Measurement with ARs

After the LoS reference measurement, we perform our main measurements with the two different-sized ARs with the same setup and procedures. In this case, we block the direct link between the Tx and Rx antennas with a wave absorber to ensure non-line-of-sight (NLoS) propagation for the Tx–Rx link and make sure that there are LoS paths for the Tx–AR and AR–Rx links. This configuration ensures that the received signal is predominantly controlled by the AR-assisted propagation path. Same as in the previous LoS measurement, we perform measurements with 16 QAM-modulated OFDM waves with 400 MHz bandwidth at the frequencies 25, 26, and 27 GHz, and obtain the results of received power and EVM. Next, we perform a faster measurement with continuous waves to evaluate the received power at more frequencies, i.e., from 24.5 GHz to 27.5 GHz. These steps are identically applied to both ARs.

It should be noted that since the size of the  $96 \times 96$ -sized AR is four times larger than the  $48 \times 48$ -sized AR, their corresponding Fraunhofer distances of the big and small ARs are 16.17 m and 4.04 m, respectively. In the measurement setup, Tx–AR and AR–Rx separations are 5.5 m and 7 m, respectively. As a result, the  $48 \times 48$ -sized AR operates in the far-field region. However, the  $96 \times 96$ -sized AR is in the radiating near-field region, where the far-field assumptions may not fully apply. Due to its narrower main scattering lobe, the larger AR exhibits higher angular sensitivity compared to the smaller AR. The simulated half power beam width (HPBW) of the  $48 \times 48$  and  $96 \times 96$ -sized ARs are 9° and 5°, respectively. Therefore, we measure the  $48 \times 48$ -sized AR at 7 different locations with a 5° step since it is enough to catch the peak power. However, the main beam for the large AR is roughly between 60° and 65°. Thus, we repeat all the previous measurements for the large AR at the previous 7 angles and additionally at 62.5°, i.e., at 8 angles in total for this AR measurement. In addition to 16 QAM-modulated waves with 400 MHz bandwidth, we also did measurements using 64 QAM-modulated waves with 100 MHz bandwidth for the large AR.

### V. Ray tracing simulation

A ray tracing simulation tool accurately evaluates the wireless communication link performance in realistic scenarios. To reproduce the measurement scenario for ray tracing simulations, we first create a 3D model of the auditorium in the software SketchUp. The front view of the 3D model is shown in Fig. 5. This model replicates the room and all

objects inside it (e.g., stairs, desks, chairs, whiteboard, lamps, windows, doors, etc.) with a 1:1 ratio. This 3D model can be exported to different formats for use in another simulation platform. For example, it can be imported into commercial ray tracing software such as Wireless InSite for ray tracing simulation. However, due to the very high complexity of the 3D room object, the simulation time is too long in Wireless InSite, especially when multiple material types are set for the objects in the room. Therefore, we choose to use the MATLAB ray tracer since it takes less simulation time and is more convenient for processing results data. The MATLAB ray tracer is a built-in commercial package, and the parameters and configurations described here enable independent reproduction using the same MATLAB tool or equivalent ray-tracing software. We exported the 3D model into “.stl” format and imported it into the MATLAB ray tracer. Since the imported room model is a whole object and cannot be edited in the ray tracer, we cannot set different material types for different objects in the room in the ray tracer even though the materials are different when we created the model in SketchUp (e.g., walls are concrete, desks are wood, chairs are fabric, etc.). Thus, the material type of the whole auditorium is set as “concrete” in the MATLAB ray tracer.

We model a horn antenna with the maximum gain of 18 dBi as Tx and Rx antennas in the ray tracer to replicate the Tx and Rx antennas in the measurement. Because the ray tracer cannot directly simulate a cascaded link from the Tx to AR and then to the Rx, we simulate the two links of Tx-AR and AR-Rx separately. The AR is modeled as an antenna in the ray tracer with two radiation patterns imported from CST simulations conducted on a periodic (infinite) array of supercells. Subsequently, finite-size array scattering patterns are derived using the embedded element approximation in CST by applying an array factor calculation on the “element pattern” of the simulated single supercell, bypassing global optimization for individual finite-sized reflectors. One pattern is towards  $+65^\circ$  direction with the normal incidence, and it is utilized when the AR functions as a Tx for the AR-Rx link. The other pattern is towards  $0^\circ$  with the  $-65^\circ$  incidence, used when the AR serves as an Rx in the Tx-AR link. The patterns obtained from CST incorporate the angle-dependent and position-dependent reflection characteristics of the surface, and take into account differences of reflection phases since it is based on the calculation of the total field scattered from all elements of the AR. Employing both patterns enables the correct mapping of spatially dependent amplitude and phase responses for each link direction, which is especially important for metasurfaces with spatially varying phase profiles. This dual-pattern approach is critical for preserving phase continuity across the Tx-RIS-Rx paths, as it ensures that the incident and scattered fields at the RIS are coherently related. Without this, simulations may yield unphysical results that misrepresent the actual EM interactions. In addition, we emphasize that the AR is modeled as

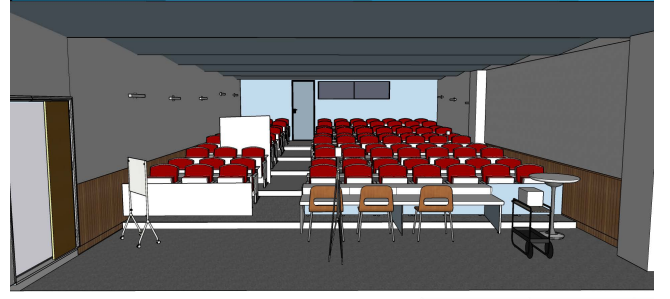


**FIGURE 5.** A front view of the 3D auditorium model, which is replicated with a 1:1 ratio from the actual sizes.

an “antenna” specifically for the MATLAB ray tracer. There is no other form to implement an AR in the ray tracer since it only allows antenna format for the Tx and Rx. But all the characteristics of this “antenna” are the CST-calculated parameters of the actual AR. It is worth noting that when we import the 3D room model, the coordinate system has to be unified for the Tx and Rx antennas, and the radiation patterns have to be rotated accordingly to fit the incidence and reflection angles.

We first run ray tracing simulations from the Tx to the AR, from which we obtain the received power at the AR. Then, the received power is used as the transmitted power at the AR for ray tracing simulations of the AR-Rx link. This assumes that the AR does not consume power itself but can reflect all the power it receives. More details of how the received power is calculated in the MATLAB ray tracer can be found in [30], which calculates the path loss and reflection loss of each propagation ray from the Tx to the Rx antenna. The received power at the Rx antenna is a coherent combination of multiple propagation rays considering their amplitudes and phases.

We place the Rx antenna at different positions from  $55^\circ$  to  $85^\circ$  and orient the main beam of the Rx antenna pattern to always face the AR. In Fig. 6, we plot the LoS paths between the Tx and the AR, and between the AR and the Rx in the MATLAB ray tracer. The locations and heights of the Tx, Rx, and AR are the same as in the measurement. For ray tracing simulations with the two ARs, we employ the shooting and bouncing rays (SBR) method. The number of diffractions is set to zero, as including them significantly increases simulation time while contributing negligibly to the received power. Only reflections are included in the simulation, where we set the maximum number of reflections to zero or three for comparison. When there is no reflection path, the ray tracer only simulates the LoS paths, as shown in Fig. 6, and the path loss calculation is based on the free-space path loss model, which is the same as in Method 2. The zero-reflection case is used to compare the simulation results with the theoretical model, and to allow for a more practical propagation environment, we set three reflection paths to compare the simulation results with the measurement results. Choosing three reflections is a good compromise between



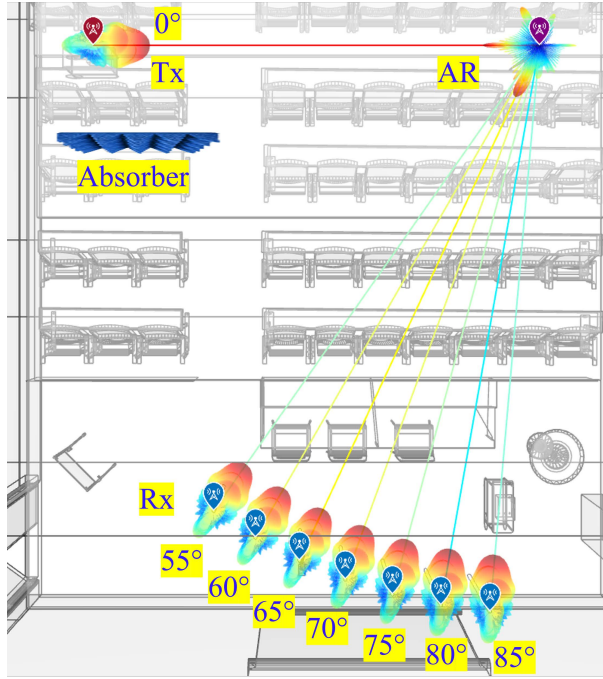


**FIGURE 6.** The Tx, Rx, and AR positions and radiation patterns in the MATLAB ray tracer, as well as the LoS paths between them.

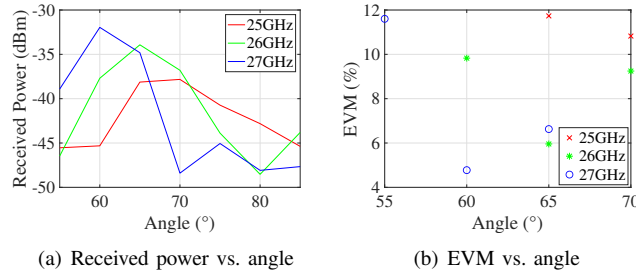


**FIGURE 7.** Measured results of the  $48 \times 48$ -sized AR with 16 QAM-modulated waves.

accurate results and computational complexity since the difference in received power from three and six reflections is less than 1 dB, which is reasonable because more reflections imply a longer propagation path and higher attenuation, and thus contribute little to the total received power, but modeling six reflections costs much more time than three reflections. Other simulation parameters are the default values in the ray tracer.

## VI. Results Analysis

In this section, we compare received power results through the AR-assisted communication links between the theoretical models, ray tracing simulations, and measurements. We analyze the AR's angular response across various Rx locations, evaluate frequency selectivity by varying frequencies, and assess spatial scalability performance through two different-sized AR prototypes.

### A. Results of the $48 \times 48$ -sized AR

From the measurements with 16 QAM-modulated waves, we obtain the received power and EVM results shown in Fig. 7(a) and Fig. 7(b), respectively. Figure 7(b) only shows the EVM values that passed the frame-averaged EVM test with the 5G NR signal (EVM less than 12.5% for 16 QAM). We observe that the maximum received power increases while the minimum EVM decreases from 25, 26, to 27 GHz. The maximum received power and minimum EVM for 25, 26, and 27 GHz occur at 70°, 65°, and 60°, respectively. The angles of the received power peaks at the three frequencies are consistent with the scattering pattern shown in Fig. 2.

Next, we use  $P_{\text{diff}}$  obtained from the reference measurement in Sec. IV-B to correct the calculated receive power from the two path loss models and from ray tracing simulations. The original powers calculated from Method 1, Method 2, and ray tracing simulations have to include the extra losses from measurement setup, i.e., the cable losses and LNA gain. For instance, the received power calculated from Method 1 is  $P_r = P_1 - L_t + G_a$  in dBm, and the received power from Method 2 is calculated as  $P_r = P_2 - L_t + G_a$  in dBm. The final corrected calculation and simulation results for the AR-assisted links are obtained by  $P_{\text{correct}} = P_r - P_{\text{diff}}$ .

The comparison of the corrected results and the measurement results with modulated waves is plotted in Fig. 8. From these three figures, we observe that the results from Method 2 and from ray tracing with zero reflection are consistent, which proves that our AR implementation method in the ray tracer is correct. Ray tracing with zero and three reflections also does not show much difference in the received power. At 25 GHz, the measurement and simulation results have very little difference at most angles, except at 60°. This is highly related to the simulated and measured scattering pattern of the AR, as we see similar circumstances in Fig. 2. At 26 GHz, the measurement results at 60°, 65°, and 70° are almost the same as the ray tracing simulation results with three reflections, which implies that our 3D model of the auditorium is accurate and the ray tracing estimation gives a similar power as in reality. In addition, at 65° (the designed reflection angle), the theoretical result for a perfect AR given by Method 1 is very close to that given by Method 2 and to the ray tracing results with zero reflection, which indicates that the 3-bit quantized lossy AR does not have much power loss at the designed reflection angle compared to a perfectly working lossless AR. At 27 GHz, the simulation results and measurement results are almost the same at 55°, 60°, and 65°. The significant differences shown at 55°, 60°, and 85° for 25 GHz, 80° and 85° for 26 GHz, and 70° to 85° for 27 GHz do not necessarily come from simulations. As shown in Fig. 7(b), the EVM results at these points exceed the acceptable threshold, indicating reduced reliability of the corresponding measurement data. At locations where the EVM results are within the threshold, simulation and

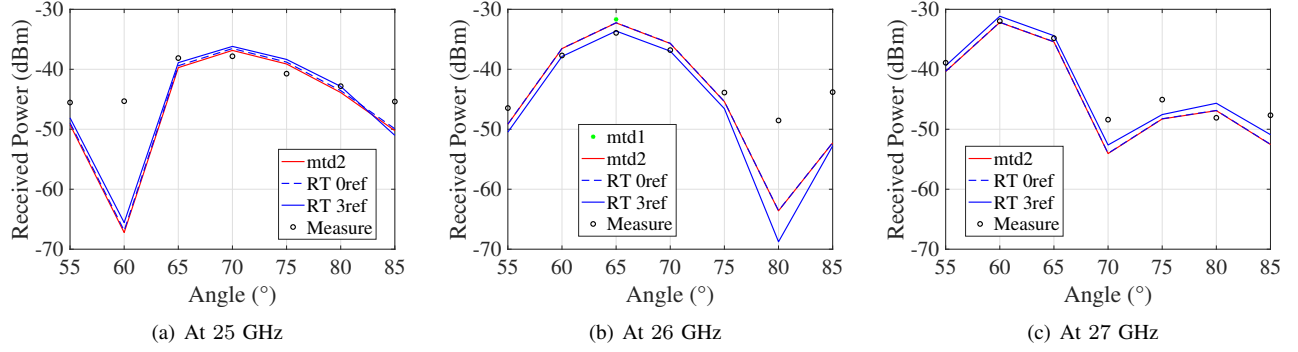


**FIGURE 8.** Results with the  $48 \times 48$ -sized AR from corrected calculation and simulation, and from measurements using the modulated waves (“mtd” indicates one of the analytical methods, “RT” represents ray tracing).

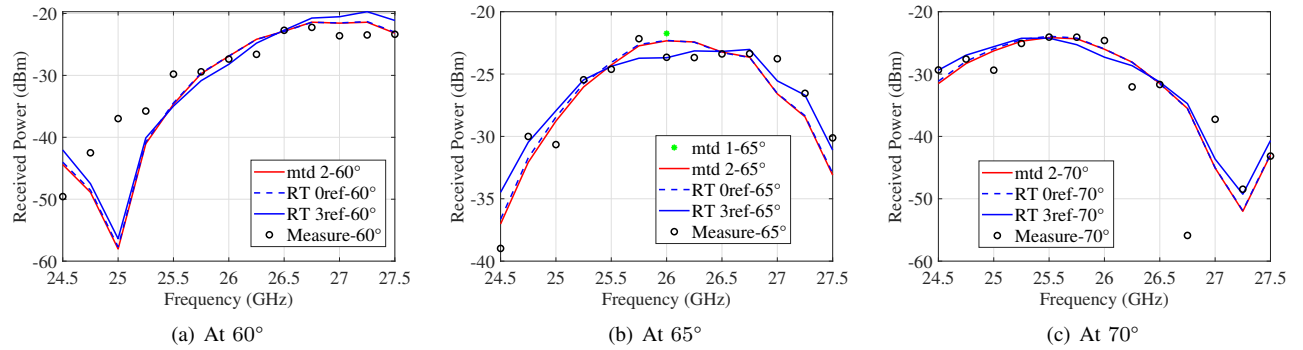


**FIGURE 9.** Results with the  $48 \times 48$ -sized AR from corrected calculation and simulation, and from measurements using the continuous waves.

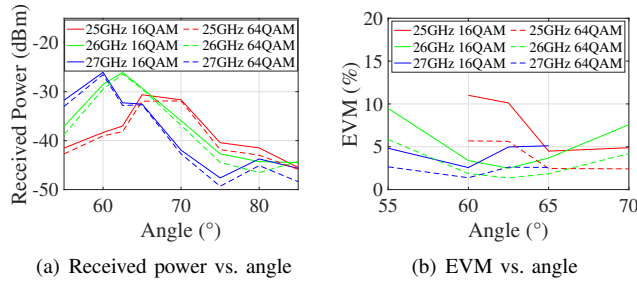


**FIGURE 10.** Measured results of the  $96 \times 96$ -sized AR with 16 QAM and 64 QAM-modulated waves.

measurement results exhibit good agreement. Therefore, it is proved that our designed AR at 26 GHz also works well at 25 and 27 GHz, with a 5° angle shift.

To evaluate the results at more frequencies, we do the same correction procedure for the continuous-wave measurement results. Here we use the continuous-wave measured results  $P_m$  and the theoretical results both from 24.5 GHz to 27.5 GHz and calculate the  $P_{diff}$  between them, the corrected results  $P_{correct}$  are from the updated  $P_{diff}$ . Since the nominal main beam direction of the AR is between 60° and 70° due to the frequency steering phenomenon, we observe the received power results at all 13 frequencies and at 60°, 65°, and 70° which are shown in Figs. 9(a)-9(c). Generally, we

achieve good agreement between the simulation results and measurements, particularly in the desired frequency band and reflection angle. There are big differences only at a few frequency points, which is related to the AR scattering pattern difference between simulations and measurements. Since 65° is the designed reflection angle, we see that the agreement at this angle is better than for 60° and 70°. In addition, we find that the “frequency steering” phenomenon limits the use of this AR for signal bandwidths greater than approximately 1 GHz. But for any individual center frequency within the given almost 3 GHz range, we can operate.

These observations confirm that our ray tracing model with the realistic AR agrees well with measurements in such an indoor scenario. Next, we can use this method to predict the communication performance of other ARs, especially those that are difficult to measure. For example, we could not measure the far-field scattering pattern of a  $96 \times 96$ -sized AR due to the limitation of the measurement setup, but we can use our models to predict the far-field performance of this AR.

## B. Results for the $96 \times 96$ -sized AR

In this section, we analyze the results for the  $96 \times 96$ -sized AR, which is a tiled combination of four pieces of the  $48 \times 48$ -sized AR. The received power and EVM results



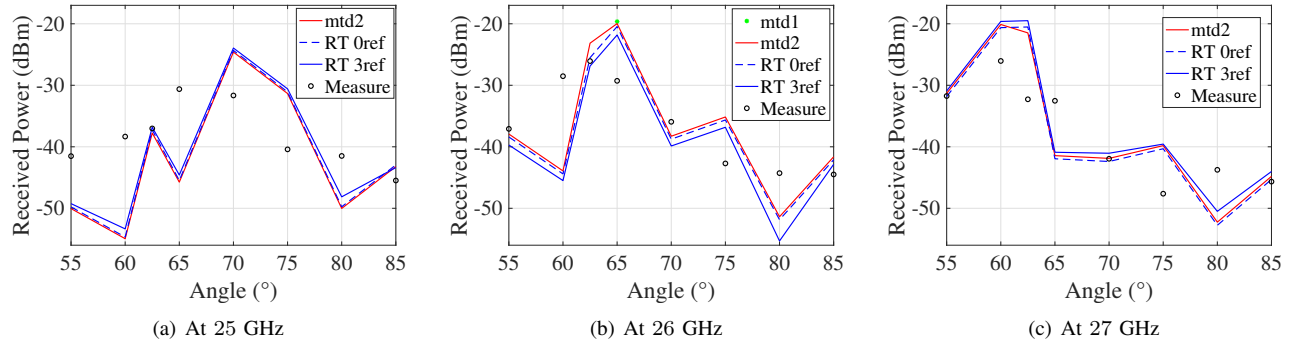


**FIGURE 11.** Results with the  $96 \times 96$ -sized AR from corrected calculation and simulation, and from measurements using the modulated waves.

for the large AR are shown in Fig. 10(a) and Fig. 10(b), respectively. We only plot the EVM results that passed the EVM tests. These results indicate that the maximum power for 25, 26, and 27 GHz appear at  $65^\circ$ ,  $62.5^\circ$ , and  $60^\circ$ , respectively. The EVM results are consistent, i.e., the minimum EVM results for the big AR also appear at the same angles for the three frequencies. The main beam direction moves to a smaller angle when increasing the frequency, which is the same as for the small AR. The only difference is that the peak power from the small AR appears at  $70^\circ$ ,  $65^\circ$ , and  $60^\circ$  for 25, 26, and 27 GHz, respectively. It also shows that the big AR works well with both 16 QAM and 64 QAM modulation schemes. When changing from 16 QAM to 64 QAM, it can achieve higher data rates and throughput. From the comparison of the results between the two modulation schemes, the 64 QAM modulation results in lower EVM and received power than using 16 QAM, but the differences are not very significant. Therefore, we only compare the simulation and calculation results with 16 QAM measurements in the following process.

The received power results from the corrected calculation and simulations, as well as from measurements using modulated waves, are shown in Fig. 11. Fig. 11(a)-11(c) display the results at 25, 26, and 27 GHz, respectively. These three figures show different beam shapes compared to the  $48 \times 48$ -sized AR. The measured power peak appears on  $62.5^\circ$ , while the simulated peak is still on  $65^\circ$  at 26 GHz. However, an interesting finding is that at some angles, the simulation and measurement results match very well, such as the power in  $62.5^\circ$  at 25 GHz and 26 GHz. According to the EVM results in Fig. 10(b), the measurement results at above  $70^\circ$  for all three frequencies, and  $55^\circ$  for 25 GHz are not so reliable since the EVM results are out of the threshold. Therefore, the simulation and measurement performance differences at these angles are not necessarily due to the simulation models. Since the beam width of the large AR is much narrower than that of the small AR, the simulation and measurement results have generally larger differences at different angles. These big differences may be due to the following reasons: 1) the accuracy of measurement is reduced due to the more

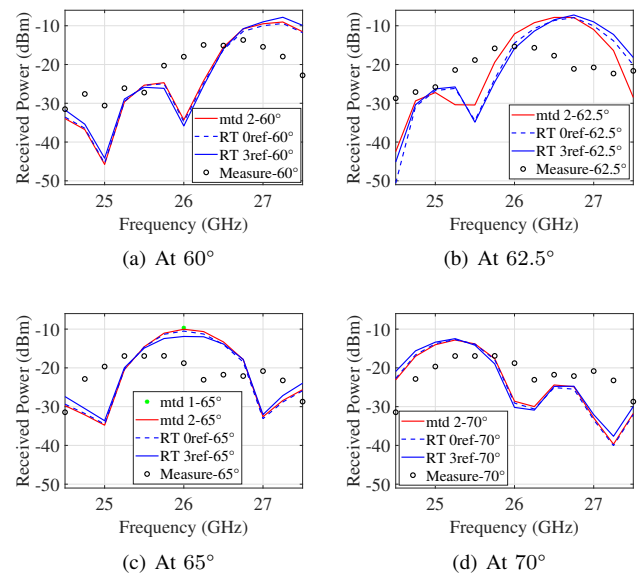


**FIGURE 12.** Results with the  $96 \times 96$ -sized AR from corrected calculation and simulation, and from measurements using continuous waves.

sensitive angular response of the large AR, and the angle samples for measurement are too sparse for this AR; 2) the simulated AR gain used in (2) and the radiation pattern used in ray tracing simulations are from a  $96 \times 96$  complete panel without discontinuity, while the measured AR is a manually combined one. Any misalignment of the unit cells from the four small ARs will reduce the total scattering efficiency of the large AR, and the copper glue at the back of the ARs may also influence reflections and the frequency selectivity of the AR; 3) the analytical expression (2) and the ray tracing simulations give far-field results for the big AR while the measured AR is in the near-field, thus the comparison between them does not match very well.

Similarly to the  $48 \times 48$ -sized AR, we compare the results corrected by continuous wave measurement. The results at the 13 frequencies are presented in Fig. 12, which again show significant differences between the simulation and measurements. These results reveal that the big AR still works

at 26 GHz, but the main beam has a slight shift, and the working bandwidth for this AR is approximately 1 GHz. It would be interesting to also compare the performance of this combined AR with a manufactured  $96 \times 96$ -sized complete AR and measure the scattering pattern of the large AR when the setup conditions allow. This will help us find out whether the differences come from the manual combining of the four ARs or from the radiation pattern differences between simulations and measurements. This work is postponed to the future as a next step.

The proposed modeling approach, while effective for many scenarios, has certain limitations. First, the scattering patterns are computed at discrete frequency sampling points, which do not fully account for the continuous frequency-dependent variations, limiting the prediction accuracy across a broad frequency range and demanding a large dataset to maintain modeling accuracy. Second, the current models do not account for near-field interactions between the antennas and ARs, which can become significant in specific scenarios, such as near-field focusing or dense multipath environments. These limitations will be addressed in future work to improve modeling accuracy and generality.

## VII. Conclusion

In this work, we introduce and study a manufactured AR that is designed to reflect normally incident plane waves toward  $65^\circ$  at 26 GHz. The scattering pattern of this AR from CST simulation and measurement is consistent in the main reflection directions. We then conduct over-the-air measurements in an auditorium with the  $48 \times 48$ -sized AR, to measure the received power at an Rx antenna through the Tx-AR-Rx link. In addition, we calculate the received power from the AR-assisted link theoretically. These results are compared with the ray tracing simulations, where we implement an AR model into the MATLAB ray tracer and simulate the actual complex propagation scenario as in the measurement. The calculated and simulated results show good agreement with the measurement results over different frequencies and different angles.

In addition, we combine four  $48 \times 48$ -sized AR panels to form a  $96 \times 96$ -sized AR and measure the received power at the Rx through anomalous reflection. Measurements at 26 GHz show a peak shift to  $62.5^\circ$  with the  $96 \times 96$ -sized AR. While the frequency response of the larger AR is slightly degraded compared to the smaller one, both simulation and measurement results exhibit good agreement across multiple angles and frequencies. These results validate the accuracy of our MATLAB ray tracer implementation for modeling ARs that can be extended to any AR type, provided their scattering patterns are available. The designed AR demonstrates wideband performance over a 2.75 GHz range and strong spatial scalability by combining multiple smaller units, achieving good performance with little deviation from the design goals without requiring a complete redesign. The proposed framework is adaptable to various

RIS or AR configurations and can be extended to outdoor or dynamic indoor scenarios, providing a cost-efficient solution for estimating wireless network performance without the need for comprehensive measurements.

## REFERENCES

- [1] V. S. Asadchy, M. Albooyeh, S. N. Tsvetkova, A. Díaz-Rubio, Y. Ra'di, and S. Tretyakov, "Perfect control of reflection and refraction using spatially dispersive metasurfaces," *Phys. Rev. B*, vol. 94, no. 7, p. 075142, Aug. 2016.
- [2] A. Díaz-Rubio, V. S. Asadchy, A. Elsakka, and S. A. Tretyakov, "From the generalized reflection law to the realization of perfect anomalous reflectors," *Science Advances*, vol. 3, no. 8, p. e1602714, Aug. 2017.
- [3] S. K. R. Vuyyuru, R. Valkonen, D.-H. Kwon, and S. A. Tretyakov, "Efficient anomalous reflector design using array antenna scattering synthesis," *IEEE Antennas Wireless Propag. Lett.*, vol. 22, no. 7, pp. 1711–1715, Jul. 2023.
- [4] M. Movahediqomi, G. Ptitcyn, and S. Tretyakov, "Comparison between different designs and realizations of anomalous reflectors for extreme deflections," *IEEE Trans. Antennas Propag.*, vol. 71, no. 10, pp. 8007–8017, Oct. 2023.
- [5] S. K. R. Vuyyuru, R. Valkonen, S. A. Tretyakov, and D.-H. Kwon, "Efficient synthesis of large finite patch arrays for scanning wide-angle anomalous reflectors," *IEEE Open J. Antennas Propag.*, vol. 6, no. 1, pp. 75–87, Feb. 2025.
- [6] A. Díaz-Rubio, S. Tsvetkova, and S. Tretyakov, "Analytical models of reflection and scattering by finite-size anomalously reflecting metasurfaces," in *Proc. 15th Eur. Conf. Antennas Propag. (EuCAP)*, 2021, pp. 1–3.
- [7] S. I. Raptis and T. V. Yioultis, "Synthesis of polarization-independent perfect anomalous reflectors via modulated metasurfaces and an analytical design model," *IEEE Trans. Microw. Theory Techn.*, vol. 71, no. 11, pp. 4703–4712, Nov. 2023.
- [8] A. M. H. Wong and G. V. Eleftheriades, "Perfect anomalous reflection with a bipartite Huygens' metasurface," *Phys. Rev. X*, vol. 8, Feb. 2018, Art. No. 011036.
- [9] D.-H. Kwon, "Lossless scalar metasurfaces for anomalous reflection based on efficient surface field optimization," *IEEE Antennas Wireless Propag. Lett.*, vol. 17, no. 7, pp. 1149–1152, Jul. 2018.
- [10] A. Díaz-Rubio and S. A. Tretyakov, "Macroscopic modeling of anomalously reflecting metasurfaces: Angular response and far-field scattering," *IEEE Trans. Antennas Propag.*, vol. 69, no. 10, pp. 6560–6571, Oct. 2021.
- [11] S. K. R. Vuyyuru, R. Valkonen, D.-H. Kwon, and S. A. Tretyakov, "Array scattering synthesis for anomalous deflection using passive aperiodic loadings," in *Proc. 18th Eur. Conf. Antennas Propag. (EuCAP)*, 2024, pp. 1–5.
- [12] V. S. Asadchy, A. Díaz-Rubio, S. N. Tsvetkova, D.-H. Kwon, A. Elsakka, M. Albooyeh, and S. A. Tretyakov, "Flat engineered multichannel reflectors," *Phys. Rev. X*, vol. 7, Sep. 2017, Art. No. 031046.
- [13] S. K. R. Vuyyuru, L. Hao, M. Rupp, S. A. Tretyakov, and R. Valkonen, "Modeling RIS from electromagnetic principles to communication systems—part I: Synthesis and characterization of a scalable anomalous reflector," *IEEE Trans. Antennas Propag.*, vol. 73, no. 3, pp. 1743–1755, Mar. 2025.
- [14] L. Hao, S. K. R. Vuyyuru, S. A. Tretyakov, A. Salihu, M. Rupp, and R. Valkonen, "Modeling RIS from electromagnetic principles to communication systems—part II: System-level simulation, ray tracing, and measurements," *IEEE Trans. Antennas Propag.*, vol. 73, no. 3, pp. 1756–1767, Mar. 2025.
- [15] J. Huang and J. A. Encinar, *Reflectarray Antennas*. Hoboken, NJ, USA: Wiley, 2008.
- [16] N. Yu, P. Genevet, M. A. Kats, F. Aieta, J.-P. Tetienne, F. Capasso, and Z. Gaburro, "Light propagation with phase discontinuities: generalized laws of reflection and refraction," *Science*, vol. 334, pp. 333–337, Oct. 2011.
- [17] Y. Jiang, F. Gao, M. Jian, S. Zhang, and W. Zhang, "Reconfigurable intelligent surface for near field communications: Beamforming and sensing," *IEEE Trans. Wireless Commun.*, vol. 22, no. 5, pp. 3447–3459, May 2023.

- [18] M. Jian, G. C. Alexandropoulos, E. Basar, C. Huang, R. Liu, Y. Liu, and C. Yuen, "Reconfigurable intelligent surfaces for wireless communications: Overview of hardware designs, channel models, and estimation techniques," *Intelligent and Converged Networks*, vol. 3, no. 1, pp. 1–32, Mar. 2022.
- [19] J. Huang, C.-X. Wang, Y. Sun, R. Feng, J. Huang, B. Guo, Z. Zhong, and T. J. Cui, "Reconfigurable intelligent surfaces: Channel characterization and modeling," *Proc. IEEE*, vol. 110, no. 9, pp. 1290–1311, Sep. 2022.
- [20] W. Tang, X. Chen, M. Z. Chen, J. Y. Dai, Y. Han, M. D. Renzo, S. Jin, Q. Cheng, and T. J. Cui, "Path loss modeling and measurements for reconfigurable intelligent surfaces in the millimeter-wave frequency band," *IEEE Trans. Commun.*, vol. 70, no. 9, pp. 6259–6276, Sep. 2022.
- [21] W. Tang, M. Z. Chen, X. Chen, J. Y. Dai, Y. Han, M. Di Renzo, Y. Zeng, S. Jin, Q. Cheng, and T. J. Cui, "Wireless communications with reconfigurable intelligent surface: Path loss modeling and experimental measurement," *IEEE Trans. Wireless Commun.*, vol. 20, no. 1, pp. 421–439, Jan. 2021.
- [22] M. Najafi, V. Jamali, R. Schober, and H. V. Poor, "Physics-based modeling and scalable optimization of large intelligent reflecting surfaces," *IEEE Trans. Commun.*, vol. 69, no. 4, pp. 2673–2691, Apr. 2021.
- [23] O. Özdoğan, E. Björnson, and E. G. Larsson, "Intelligent reflecting surfaces: Physics, propagation, and pathloss modeling," *IEEE Wireless Commun. Lett.*, vol. 9, no. 5, pp. 581–585, May 2020.
- [24] V. Degli-Esposti, E. M. Vitucci, M. D. Renzo, and S. A. Tretyakov, "Reradiation and scattering from a reconfigurable intelligent surface: A general macroscopic model," *IEEE Trans. Antennas Propag.*, vol. 70, no. 10, pp. 8691–8706, Oct. 2022.
- [25] E. M. Vitucci, M. Albani, S. Kodra, M. Barbiroli, and V. Degli-Esposti, "An efficient ray-based modeling approach for scattering from reconfigurable intelligent surfaces," *IEEE Trans. Antennas Propag.*, vol. 72, no. 3, pp. 2673–2685, Mar. 2024.
- [26] L. Hao, F. S. Cuesta, and S. A. Tretyakov, "Comparison of simplistic system-level RIS models and diffraction-theory solutions," in *Proc. 18th Eur. Conf. Antennas Propag. (EuCAP)*, 2024, pp. 1–5.
- [27] S. Kosulnikov, F. S. Cuesta, X. Wang, and S. A. Tretyakov, "Simple link-budget estimation formulas for channels including anomalous reflectors," *IEEE Trans. Antennas Propag.*, vol. 71, no. 6, pp. 5276–5288, Jun. 2023. Corrections: vol. 72, no. 6, p. 5432, Jun. 2024.
- [28] C. A. Balanis, *Antenna Theory: Analysis and Design*. John Wiley & sons, 2015.
- [29] S. W. Ellingson, "Path loss in reconfigurable intelligent surface-enabled channels," in *2021 IEEE 32nd Annual International Symposium on Personal, Indoor and Mobile Radio Communications (PIMRC)*, 2021, pp. 829–835.
- [30] L. Hao, F. S. Cuesta, S. A. Tretyakov, and M. Rupp, "Improving propagation channels with static scatterers," *IEEE Antennas Wireless Propag. Lett.*, vol. 23, no. 6, pp. 1924–1928, Jun. 2024.





**Le Hao** (Member, IEEE) received a B.Eng. degree in Electronics Science and Technology and an M.Eng. degree in Control Science and Engineering from Tongji University, China, in 2017 and 2020, respectively. She received a Dr. Techn. degree in Telecommunications from Technische Universität Wien (TU Wien), Austria, in 2024. She is currently a postdoctoral researcher at the Institute of Telecommunications at TU Wien. Her research interests include reconfigurable intelligent surfaces (RIS), ray tracing, signal processing, and reinforcement learning in mobile communication systems.



**Risto Valkonen** (Member, IEEE) received the M.Sc. (Tech.) degree in communications engineering and the D.Sc. (Tech.) degree in electrical engineering from Aalto University, Finland, in 2007 and 2013, respectively. From 2006 to 2013, he was with the Department of Radio Science and Engineering, Aalto University. From 2013 to 2015, he was Postdoctoral Researcher with the University of Kiel. Since 2015, he has been with Nokia and since 2016 with Nokia Bell Labs as Antenna Specialist. His research interest includes antennas and RF front-ends for future communication systems.



**Sravan Kumar Reddy Vuyyuru** (Member, IEEE) received a B.Tech degree from the Hindustan Institute of Technology & Science (HITS), Chennai, India, in 2018 and a joint diploma M.S. degree from the Erasmus Mundus Innovative Microwave Electronics and Optics (EMIMEO) master program in the University of Limoges, Limoges, France, and the University of Brescia, Brescia, Italy, in 2021. He is currently a Marie Skłodowska Curie fellow with the MetaWireless project working at Nokia Bell Labs, Oulu, Finland, and pursuing

a Ph.D. degree under the supervision of Prof. Sergei A. Tretyakov with the Department of Electronics and Nanoengineering, School of Electrical Engineering, Aalto University, Espoo, Finland. His research interests include applied electromagnetics, antennas, ray tracing, and reconfigurable intelligent surfaces for anomalous reflection and sensing for wireless integrated sensing and communications, especially in the mmWave range.



**Sergei A. Tretyakov** (Fellow, IEEE) received the Dipl. Engineer-Physicist, Ph.D., and D.Sc. degrees in radiophysics from Saint Petersburg State Technical University, Saint Petersburg, Russia, in 1980, 1987, and 1995, respectively.

From 1980 to 2000, he was with the Radiophysics Department, Saint Petersburg State Technical University. He is currently a Professor of radio science with the Department of Electronics and Nanoengineering, Aalto University, Espoo, Finland. He has authored or coauthored six research

monographs and more than 370 journal articles. His current research interests include electromagnetic field theory, complex media electromagnetics, metamaterials, and microwave engineering.

Dr. Tretyakov served as the General Chair of the International Congress Series on Advanced Electromagnetic Materials in Microwaves and Optics (Metamaterials) from 2007 to 2013. He served as the President of the Virtual Institute for Artificial Electromagnetic Materials and Metamaterials (Metamorphose VI). He served as the Chairperson of the St. Petersburg IEEE Electron Devices (ED)/Microwave Theory and Techniques (MTT)/Antennas & Propagation (AP) Chapter from 1995 to 1998.



**Markus Rupp** (Fellow, IEEE) received the Dipl.Ing. degree from the University of Saarbrücken, Germany, in 1988, and the Dr.Ing. degree from Technische Universität Darmstadt, Germany, in 1993. Until 1995, he held a postdoctoral research position with the University of California at Santa Barbara, Santa Barbara, CA, USA. From 1995 to 2001, he was with the Nokia Bell Laboratories, Wireless Technology Research Department, Holmdel, NJ, USA. Since 2001, he has been a Full Professor in digital signal processing in mobile

communications with TU Wien.